Fe I Lines in 0.91–1.33 μm Spectra of Red Giants for Measuring the Microturbulence and Metallicities

Sohei Kondo[1], Kei Fukue[1], Noriyuki Matsunaga[1,2], Yuji Ikeda[1,3] , Daisuke Taniguchi[2], Naoto Kobayashi[1,4,5],
Hiroaki Sameshima[1] , Satoshi Hamano[1], Akira Arai[1], Hideyo Kawakita[1,6], Chikako Yasui[1,7], Natsuko Izumi[7] ,
Misaki Mizumoto[8] , Shogo Otsubo[6], Keiichi Takenaka[6], Ayaka Watase[6], Akira Asano[6], Tomohiro Yoshikawa[9], and
Takuji Tsujimoto[7]

[1] Laboratory of Infrared High-resolution spectroscopy (LiH), Koyama Astronomical Observatory, Kyoto Sangyo University, Motoyama, Kamigamo, Kita-ku, Kyoto 603-8555, Japan; kondo@ioa.s.u-tokyo.ac.jp
[2] Department of Astronomy, Graduate School of Science, The University of Tokyo, 7-3-1 Hongo, Bunkyo-ku, Tokyo 113-0033, Japan
[3] Photocoding, 460-102 Iwakura-Nakamachi, Sakyo-Ku, Kyoto 606-0025, Japan
[4] Kiso Observatory, Institute of Astronomy, School of Science, The University of Tokyo, 10762-30 Mitake, Kiso-machi, Kiso-gun, Nagano 397-0101, Japan
[5] Institute of Astronomy, Graduate School of Science, The University of Tokyo, 2-21-1 Osawa, Mitaka, Tokyo 181-0015, Japan
[6] Department of Physics, Faculty of Science, Kyoto Sangyo University, Motoyama, Kamigamo, Kita-ku, Kyoto 603-8555, Japan
[7] National Astronomical Observatory of Japan, 2-21-1 Osawa, Mitaka, Tokyo 181-0015, Japan
[8] Centre for Extragalactic Astronomy, Department of Physics, University of Durham, South Road, Durham DH1 3LE, UK
[9] Edechs, 17203 Iwakura-Minami-Osagi-cho, Sakyo-ku, Kyoto 606-0003, Japan
Received 2018 October 3; revised 2019 March 2; accepted 2019 March 3; published 2019 April 23

Abstract

For a detailed analysis of stellar chemical abundances, high-resolution spectra in the optical have mainly been used, while the development of near-infrared (NIR) spectrograph has opened new wavelength windows. Red giants have a large number of resolved absorption lines in both the optical and NIR wavelengths, but the characteristics of the lines in different wave passbands are not necessarily the same. We present a selection of Fe I lines in the z', Y, and J bands (0.91–1.33 μm). On the basis of two different lists of lines in this range, the Vienna Atomic Line Database (VALD) and the catalog published by Meléndez & Barbuy in 1999 (MB99), we selected sufficiently strong lines that are not severely blended and compiled lists with 107 Fe I lines in total (97 and 75 lines from VALD and MB99, respectively). Combining our lists with high-resolution ($\lambda/\Delta\lambda = 28{,}000$) and high signal-to-noise (>500) spectra taken with an NIR spectrograph, WINERED, we present measurements of the iron abundances of two prototype red giants: Arcturus and μ Leo. A bootstrap method for determining the microturbulence and abundance together with their errors is demonstrated. The standard deviations of $\log \epsilon_{\mathrm{Fe}}$ values from individual Fe I lines are significantly smaller when we use the lines from MB99 instead of those from VALD. With the MB99 list, we obtained $\xi = 1.20 \pm 0.11$ km s^{-1} and $\log \epsilon_{\mathrm{Fe}} = 7.01 \pm 0.05$ dex for Arcturus, and $\xi = 1.54 \pm 0.17$ km s^{-1} and $\log \epsilon_{\mathrm{Fe}} = 7.73 \pm 0.07$ dex for μ Leo. These final values show better agreements with previous values in the literature than the corresponding values we obtained with VALD.

Key words: stars: abundances – stars: individual (Arcturus, μ Leo) – stars: late-type – techniques: spectroscopic

Supporting material: machine-readable tables

1. Introduction

Recent developments in instruments (e.g., multi-object spectrographs) and statistical approaches (e.g., CANNON, Ness et al. 2015; ASPCAP, García Pérez et al. 2016) provide opportunities to measure metallicities of a larger number of stars and/or to higher precision. Among the various methods available for estimating stellar metallicities, the measurement of individual metallic lines in high-resolution spectra is the most direct and fundamental one. Such detailed analyses of high-resolution spectra have mostly been performed with optical spectra, while recently developed instruments now produce near-infrared (NIR) high-resolution spectra that are similarly useful and high in quality. For example, the APOGEE project established fiber-fed multiobject spectrographs to collect hundreds of H-band spectra (1.5–1.7 μm, $\lambda/\Delta\lambda = 22{,}500$) simultaneously (Majewski et al. 2017). Several other NIR spectrographs with a single slit have been used for abundance analysis for individual stars, especially those affected by strong interstellar extinction. Such pioneering works include studies of chemical abundances of stars in the Galactic bulge (Carr et al. 2000; Cunha & Smith 2006;

Ryde et al. 2009, 2010, 2016) and red supergiants in clusters in the inner disk (Davies et al. 2009a, 2009b; Origlia et al. 2013, 2016).

Since abundance analyses based on NIR spectra have now turned state of the art, they require, e.g., accurate calibration of oscillator strengths of absorption lines in that spectral domain. For example, the APOGEE project has not only measured the abundances of a large number of stars but has also made progress in establishing methodology and fundamental data sets: a list of absorption lines in the H band (Shetrone et al. 2015), a new grid of atmospheric models (Mészáros et al. 2012), a tool to search for the best sets of stellar parameters (García Pérez et al. 2016), and so on. In particular, an accurate line list is essential to perform chemical analysis in stellar atmospheres. The correct identification of lines is mandatory, and estimates of abundances cannot be accurately carried out without accurate oscillator strengths. As Ryde et al. (2009) pointed out, many lines in the NIR are not properly identified or lack well-calibrated oscillator strengths. Available line lists with a wide wavelength coverage include Kurucz's database (Kurucz & Bell 1995), Vienna Atomic Line Database

(VALD3; Ryabchikova et al. 2015), and the list published by Meléndez & Barbuy (1999; hereinafter referred to as MB99). MB99 compiled absorption lines, which they identified in the solar spectrum, and obtained astrophysical $\log g f$ values.[10] In contrast, Kurucz's database and VALD3 have a significantly larger number of lines including those only theoretically predicted. In this work, we compared results of abundance analysis obtained with lines in the range of 0.91–1.33 μm from VALD3 and the MB99 list, and also compared our measurements with previous results.

In addition to comparing line lists, another goal of this study is to test the determination of the microturbulence, ξ, using NIR high-resolution spectra. In an abundance analysis of stars, ξ is one of the most important parameters, and its uncertainty often remains a major error source for the metallicity. In a classical analysis of optical high-resolution spectra, ξ is estimated by necessitating that $\log \epsilon_{\mathrm{Fe}}$, defined as $\log(N_{\mathrm{Fe}}/N_{\mathrm{H}}) + 12$, from individual lines shows no dependency on line strengths, e.g., equivalent widths (EWs, denoted as W) or reduced EWs (W/λ). This method requires a large number of iron lines with various strengths. For NIR spectra, different methods for estimating ξ have often been used so far. Davies et al. (2009b), for example, obtained it by comparing the molecular bands in synthetic and observed spectra. Sometimes ξ is assumed a priori. In an analysis of more than 10^5 stars in the APOGEE project, ξ for giants were estimated from the relationship between the surface gravity and ξ in DR13 and by comparing observed spectra to libraries of theoretical spectra in DR14 (Holtzman et al. 2018).[11] In contrast, Smith et al. (2013) estimated ξ with H-band spectra in the same manner as the classical method mentioned above. However, the number of iron lines used was small (eight or nine), and the range of their strengths was limited. As shown below, we can identify more lines with a broad range of strengths at 0.91–1.33 μm.

2. Observation and Data Reduction

We investigated WINERED spectra of well-studied red giants, Arcturus and μ Leo. The former has a subsolar metallicity, and the latter is significantly metal-rich; previous estimates are summarized in Section 3.1. WINERED has a spectral resolution of $R \equiv \lambda/\Delta\lambda \sim 28{,}000$. A single exposure covers a wide wavelength range of 0.91–1.35 μm, which includes the z', Y, and J bands (Ikeda et al. 2016). Such a wide coverage is a huge advantage in abundance analysis. A large number of Fe I lines are included, and their strengths range from a severely saturated regime to a very weak regime, thus allowing accurate estimates of ξ.

We observed Arcturus and μ Leo on 2013 February 23 with WINERED mounted on the Nasmyth focus of the 1.3 m Araki Telescope at Koyama Astronomical Observatory, Kyoto Sangyo University, Japan (Table 1). WINERED is a cross-dispersed-type echelle spectrograph using a 1.7 μm cutoff 2048 × 2048 HAWAII-2RG array. The pixel scale is $0{\farcs}8$ pixel^{-1}, and we used a slit $48''$ in length and $1{\farcs}6$ in width, providing a spectral resolution of $R \sim 28{,}000$ (further technical details are described in Ikeda et al. 2016). We also observed HIP 76267 (A1IV) as a telluric standard. The total exposure times were 20, 240, and 600 s for Arcturus, μ Leo, and HIP 76267, respectively. For every object, sky frames without the target or any other visible stars included in the slit were

obtained to subtract the background including bias and dark of the detector as well as the sky and ambient radiation.

All the data were reduced following standard procedures adopted in the WINERED pipeline (Hamano et al. in preparation) that is established using PyRAF,[12] which calls IRAF tasks,[13] including sky subtraction, scattered light subtraction, flat-fielding (using a halogen lamp with an integrating sphere), geometric transformation, aperture extraction, and wavelength calibration based on Th–Ar lamp spectra. The continuum was traced in each echelle order and normalized to unity. After the pipeline reduction, we applied the method described in Sameshima et al. (2018) for the telluric correction. The spectrum of a telluric standard, HIP 76267, with a high signal-to-noise ratio (S/N $\sim$ 1200), was used for both Arcturus and μ Leo. The spectra in different echelle orders were then combined by taking the averages at overlapping wavelengths, and thus we obtained the continuum-normalized continuous spectra of Arcturus and μ Leo for the z', Y, and J bands. The wavelength ranges of the three bands, in which the telluric lines can be well corrected, cover 0.91–0.93, 0.96–1.115, and 1.16–1.33 μm, respectively. Finally, the stellar redshifts were corrected so that the absorption lines can be directly compared with those in synthetic spectra in rest air wavelength. We estimated the S/N ratios at around 12,500 Å, as given in Table 1, in a manner similar to that described in Fukue et al. (2015). Considering the noise present in the telluric correction, we also calculated the S/N of the spectra after the correction. The reduced spectra of Arcturus and μ Leo are presented in Figure 1.

3. Tools and Basic Data

3.1. Atmosphere Models and Stellar Parameters

For the abundance analysis, we used SPTOOL developed by Y. Takeda (2011, private communication), which utilizes the

Table 1
Targets and WINERED Observations

Object	Arcturus	μ Leo
Alias	HD 124897, α Boo	HD 85503
T_{eff} (K)[a]	4286 ± 35	4474 ± 60
$\log g$ (dex)[a]	1.64 ± 0.06	2.51 ± 0.09
[M/H] (dex)[a]	−0.52 ± 0.08	0.25 ± 0.15
Date (UT)	2013 Feb 23	2013 Feb 23
Time (UT)	16:23	17:18
Exposures (s)	20 (2 s × 10)	240 (20 s × 12)
S/N[b]	1200	900
S/N[b c]	850	720

Notes.
[a] The stellar parameters are adopted from Heiter et al. (2015). For [M/H], we simply use their [Fe/H].
[b] S/N is measured around the middle of J band. Note that these S/N consider statistical errors measured by comparing multiple integrations.
[c] After the correction of telluric lines with a spectrum (S/N = 1200) of the telluric standard HIP 76267.

---

[10] Here and elsewhere in this paper, we consider the logarithm to base 10.
[11] http://www.sdss.org/dr14/irspec/

[12] PyRAF is a product of the Space Telescope Science Institute, which is operated by AURA for NASA.
[13] IRAF is distributed by the National Optical Astronomy Observatories, which are operated by the Association of Universities for Research in Astronomy, Inc., under cooperative agreement with the National Science Foundation.
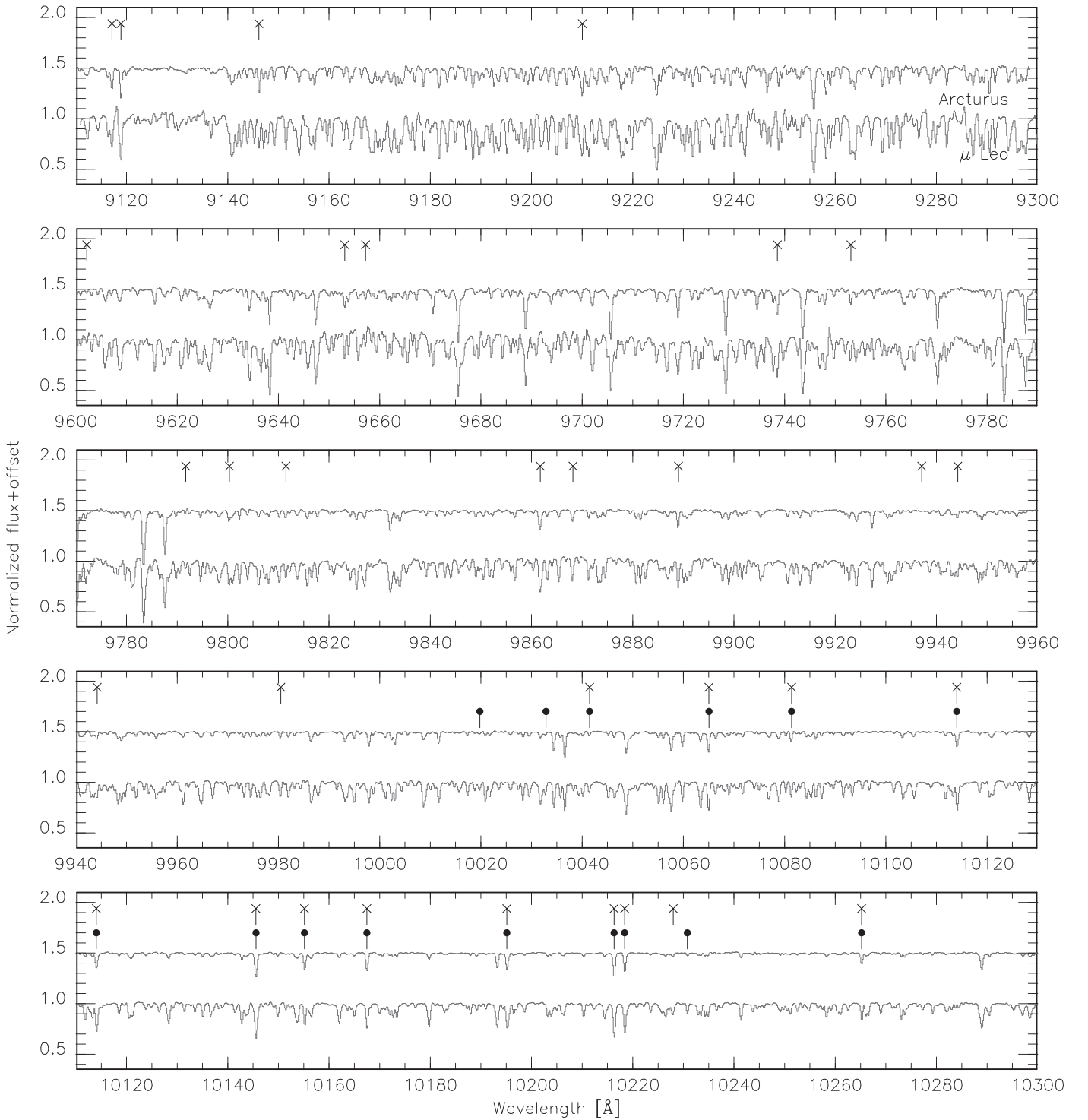
Figure 1. Reduced spectra of Arcturus and μ Leo after the telluric correction. The short lines with the cross symbols and the filled circles indicate Fe I lines selected from VALD3 and MB99, respectively, for the metallicity measurements for Arcturus and/or μ Leo.

ATLAS9/WIDTH9 codes by R. L. Kurucz (Kurucz 1993). This tool synthesizes model spectra using ATLAS9 model atmospheres for a given set of parameters, including effective temperature ($T_{\rm eff}$), surface gravity ($\log g$), and global metallicity ([M/H] or $\log Z/Z_\odot$). In these tools and models, the solar abundance was assumed to be that of Anders & Grevesse (1989). However, in the following discussions, we translate $\log \epsilon_{\rm Fe}$ values into [Fe/H] by adopting 7.45 dex (Grevesse et al. 2007) as the solar $\log \epsilon_{\rm Fe}$

value, which was also adopted in many recent works (Smith et al. 2013; Jofré et al. 2014).

We adopted the basic stellar parameters and their errors of the two targets, as listed in Table 1, from Heiter et al. (2015). We simply use their [Fe/H] values as [M/H] in the atmosphere models. For comparison, Figure 2 plots previous estimates of $T_{\rm eff}$, $\log g$, and [Fe/H], published after 1970, against the publication date. We included only papers with [Fe/H] in
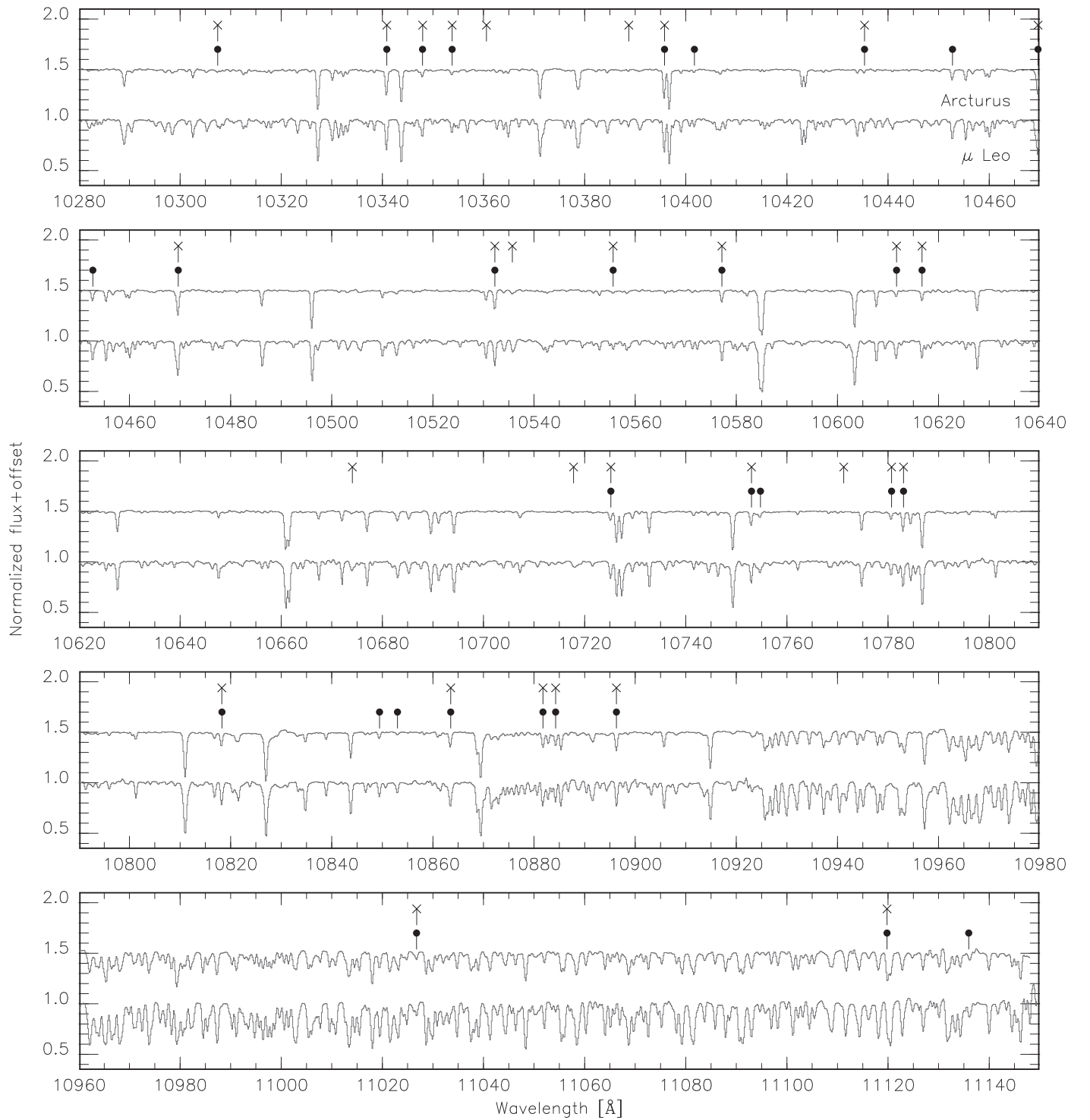
Figure 1. (Continued.)

which the assumed solar $\log \epsilon_{\mathrm{Fe}}$ was clearly given and those with iron abundance given as $\log \epsilon_{\mathrm{Fe}}$, and all the [Fe/H] values in Figure 2 are scaled with the solar $\log \epsilon_{\mathrm{Fe}}$ of 7.45 dex. The averages of the values published in 2000 or later (18 and 6 papers for Arcturus and μ Leo, respectively) give (with standard deviations in parentheses), $T_{\mathrm{eff}} = 4279$ K (40 K), $\log g = 1.60$ dex (0.18 dex), and [Fe/H] $= -0.51$ dex (0.06 dex) for Arcturus, and $T_{\mathrm{eff}} = 4520$ K (43 K), $\log g = 2.36$ dex (0.22 dex), and [Fe/H] $= +0.33$ dex

(0.06 dex) for μ Leo. These averages agree well with the parameters from Heiter et al. (2015) in Table 1.

3.2. Line Lists of VALD3 and MB99

VALD3 has a large collection of atomic lines, including more than 10,000 Fe I lines, and molecular lines covering the wavelength range of the z', Y, and J bands. In our spectrum of Arcturus, Y. Ikeda et al. (2019, in preparation) identified the atomic lines of various species, including more than 300 Fe I
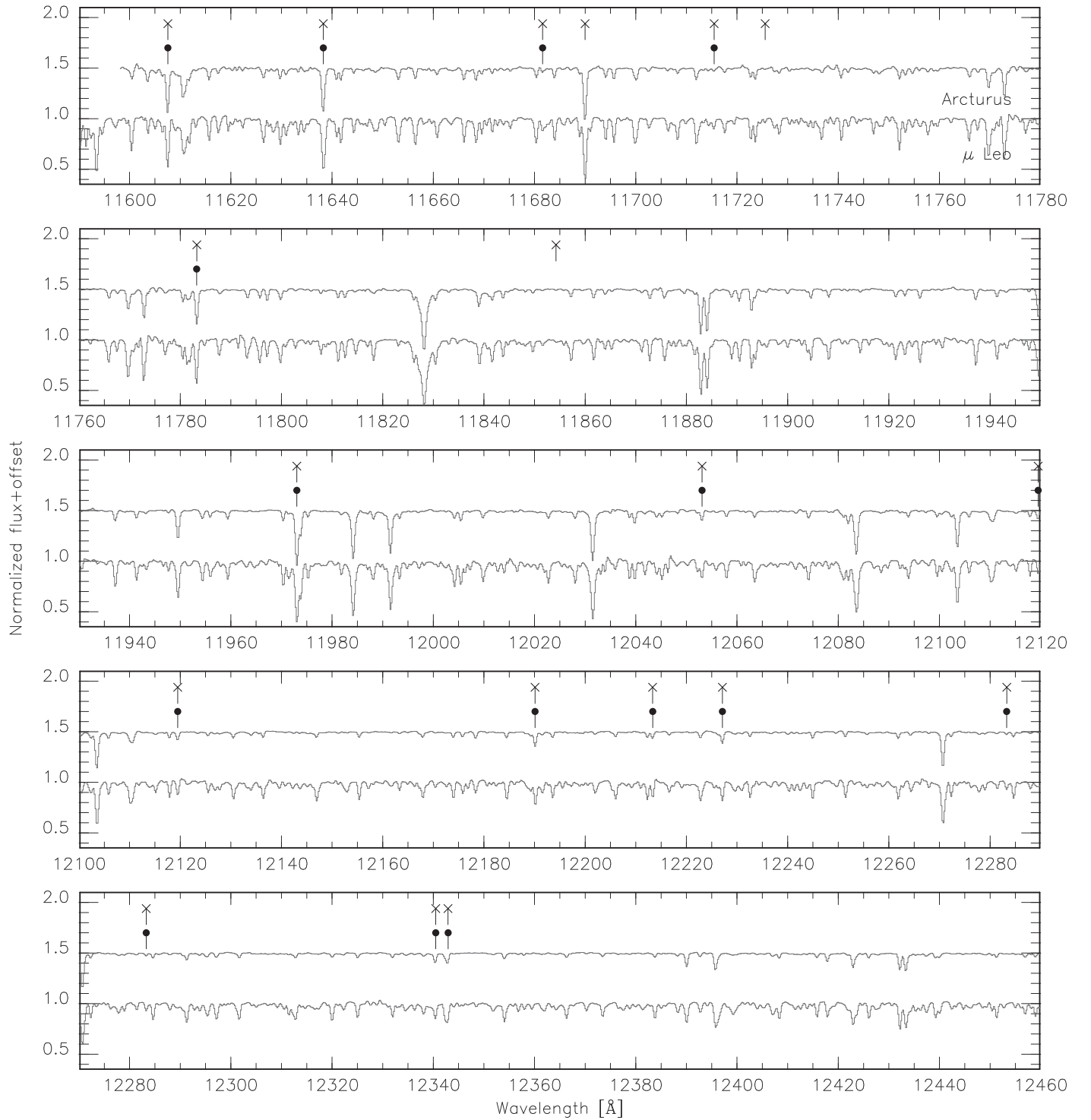
Figure 1. (Continued.)

lines (see a summary in Taniguchi et al. 2018). We also considered the line list of MB99, which includes 363 Fe I lines in the 1.00–1.34 μm range among ∼1000 atomic lines in total. We note that MB99 contains lines at only $\lambda > 1 \mu$m and does not cover the entire range of WINERED spectra. There are 159 lines in both the list of Y. Ikeda et al. (2019, in preparation) and that of MB99, and there are 475 lines in at least one of the two lists. The wavelength and the excitation potential (EP in eV) of each line are consistent between the two line lists. In contrast,

the log gf values in the two lists are significantly different, as seen below.

Fe II lines are not used in our analysis, although there are more than 10,000 Fe II lines in VALD3 in the same wavelength range. MB99 lists 13 Fe II lines, all of which are also included in VALD3. We have in fact identified a few Fe II lines in Arcturus (to be reported in Y. Ikeda et al. 2019, in preparation) and/or μ Leo. However, most of them are weaker than 0.01, and none of them are stronger than 0.05 in depth. Therefore, we
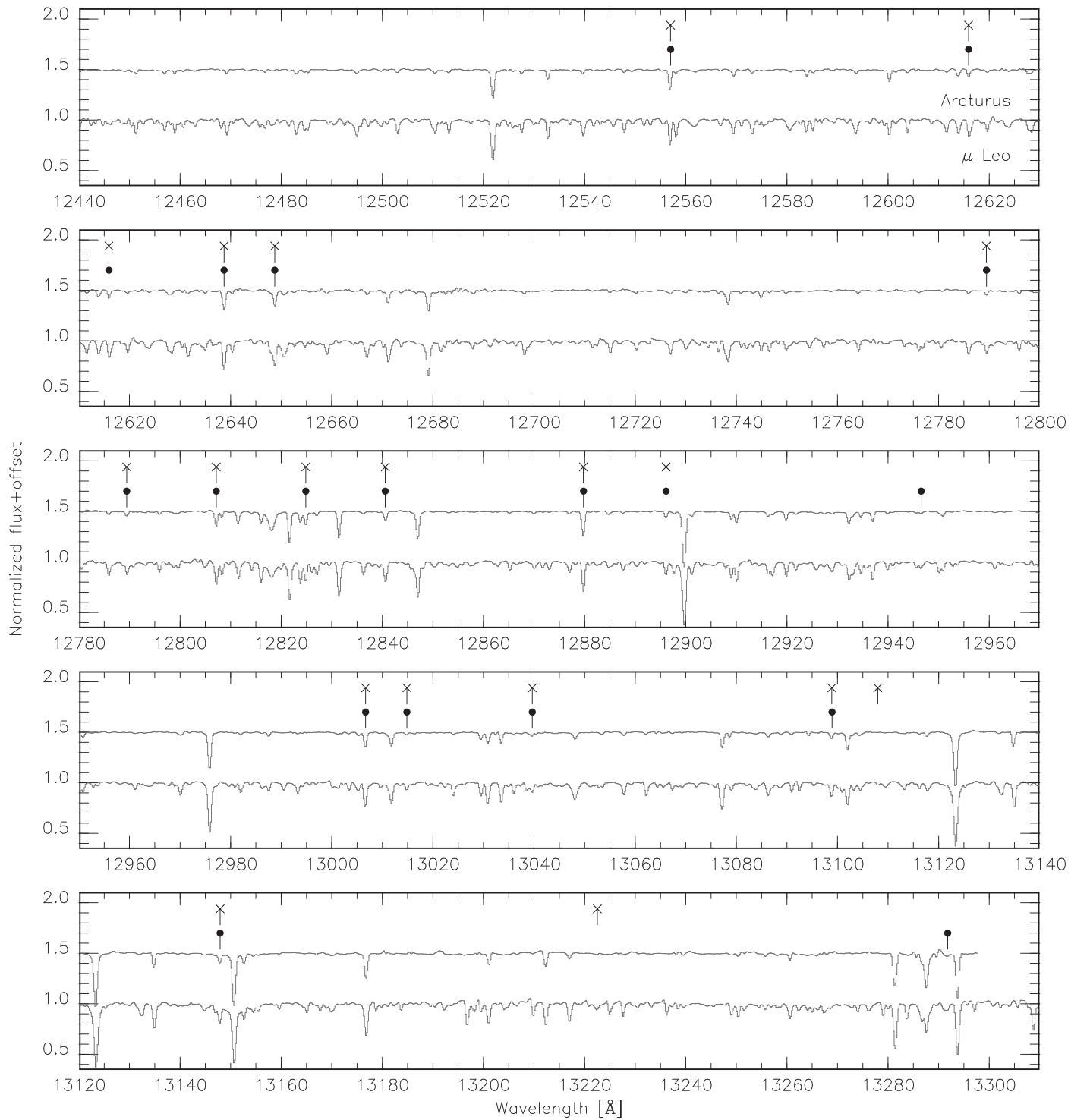
Figure 1. (Continued.)

focus on abundance measurements using only Fe I lines in this paper. We use synthetic spectra for both the selection of Fe I lines and the abundance measurements, and we include all the lines in VALD3 or MB99 (i.e., not only the Fe I lines selected in Y. Ikeda et al. 2019, in preparation). We use VALD3 for atomic lines when we consider Fe I lines and their parameters given in VALD3, and the same is true for the MB99 lines, in order to avoid mixing the two lists in our spectral analysis. In both cases, we adopt lines of CN, CO, C$_2$, CH, and OH

molecules in VALD3 because MB99 compiled only atomic lines.

4. Selection of Fe I Lines

To find good Fe I lines for measuring iron abundances, we started the line selection from the aforementioned 475 Fe I lines. First, we excluded 32 lines in the following three ranges, as they are severely affected by telluric lines: 9300–9600 Å, 11,150–11,600 Å, and longer than 13,300 Å. Then, we
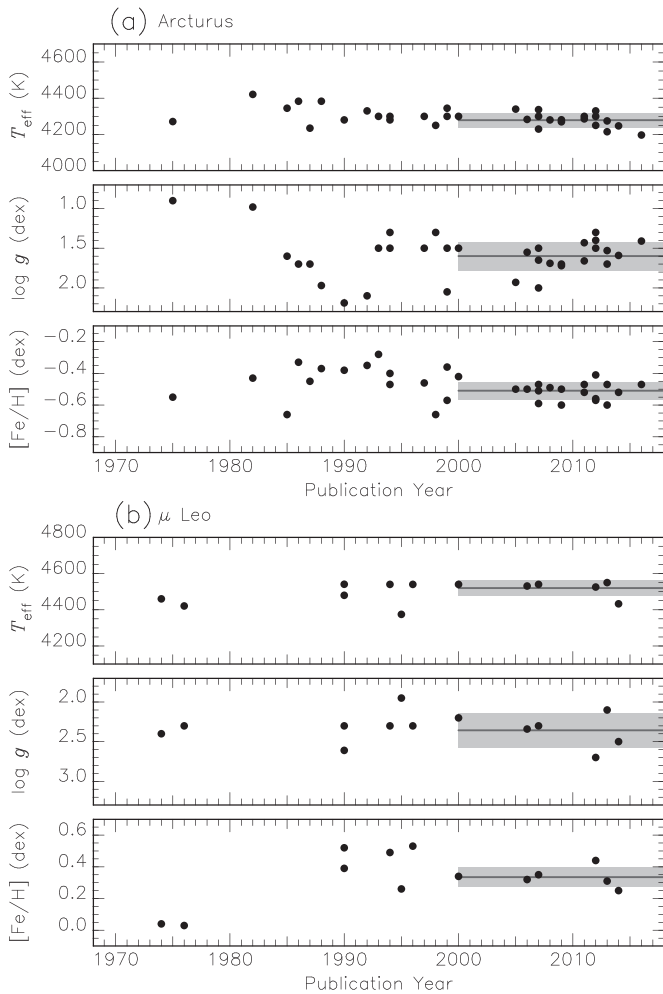
Figure 2. Previous measurements of T_{eff}, $\log g$, and [Fe/H] in the literature. The upper panels consider 33 papers for Arcturus (Maeckle et al. 1975; Gratton et al. 1982; Bell et al. 1985; Kyrolainen et al. 1986; Leep et al. 1987; Edvardsson 1988; McWilliam 1990; Brown & Wallerstein 1992; Peterson et al. 1993; McWilliam & Rich 1994; Sneden et al. 1994; Hill 1997; Gonzalez & Wallerstein 1998; Tomkin & Lambert 1999; Thévenin & Idiart 1999; Carr et al. 2000; Luck & Heiter 2005; Fulbright et al. 2006; Lecureur et al. 2007; Hekker & Meléndez 2007; Ramírez et al. 2007; Meléndez et al. 2008; Worley et al. 2009; Takeda et al. 2009; Ramírez & Allende Prieto 2011; Bruntt et al. 2011; Sheffield et al. 2012; Britavskiy et al. 2012; Thygesen et al. 2012; Ramírez et al. 2013; Smith et al. 2013; Jofré et al. 2014; Boeche & Grebel 2016). The bottom panels consider 13 papers for μ Leo (Oinas 1974; Peterson 1976; McWilliam 1990; Gratton & Sneden 1990; McWilliam & Rich 1994; Luck & Challener 1995; Castro et al. 1996; Smith & Ruck 2000; Fulbright et al. 2006; Lecureur et al. 2007; Thygesen et al. 2012; Smith et al. 2013; Jofré et al. 2014). The horizontal line and strip in each panel indicate the average and standard deviation of the measurements made in 2000 or later.

measured the depths (minima measured from the normalized continuum) and central wavelengths of the lines in the synthetic spectra for the two objects (Arcturus and μ Leo). We applied the line broadening, including both macroturbulent and instrumental broadening, corresponding to $R = 28{,}000$, for the analysis in this section. If the depth of a line was shallower than 0.05, the line was rejected. We also rejected lines that show no minimum in the synthetic spectra for the two objects within 5 km s^{-1} around the expected wavelength. Such lines with a biased minimum may be strongly blended with other lines. In addition, when two or more Fe I lines were detected within 45 km s^{-1}, we included only the strongest line if its X value was larger than those of the other neighboring Fe I lines

by more than 0.5 dex; otherwise, we rejected both lines. The X index is defined as $X \equiv \log g f - \mathrm{EP} \times \theta_{exc}$, where $\theta_{exc} \equiv 5040/(0.86 \times T_{eff})$. It is a convenient indicator of line strength (Magain 1984; Gratton et al. 2006). In total, 181 (166 in VALD3 and 118 in MB99) lines in VALD3 and/or MB99 met these criteria.

Then, the impact of blending on each line observed for each object was examined and used for further selection. We estimated two EWs, W_1 and W_2, around a target line (λ_c) in a synthetic spectrum, f_{syn}:

$$W_i = \int_{\lambda_c - \Delta_i/2}^{\lambda_c + \Delta_i/2} \{1 - f_{syn}(\lambda)\} d\lambda. \tag{1}$$

For the EW of the target line itself and contaminations of lines in neighboring wavelengths, we consider two different integration ranges, Δ_1 and Δ_2, which correspond to velocities of 30 and 60 km s^{-1}, respectively. Neighboring lines other than the target line can also contribute to these EWs (W_1 and W_2). In addition, to evaluate the contamination, we constructed synthetic spectra, $f_{syn}^{\dagger}$, with the target Fe I line removed from the line lists for each of the two stars. The EW of contaminating lines, $W_i^{\dagger}$, can be estimated by considering Equation (1) but with f_{syn} replaced by $f_{syn}^{\dagger}$. Combining these EWs, we consider two indices,

$$\beta_1 = W_1^{\dagger}/W_1, \tag{2}$$

$$\beta_2 = (W_2^{\dagger} - W_1^{\dagger})/W_1, \tag{3}$$

as indicators of blending. The former measures the contamination to the main part of each target line, and the latter measures the contamination mainly to the continuum part around the line. First, we rejected lines for which $f_{syn}^{\dagger} - f_{syn}$ does not exceed 0.05. The 181 lines were selected because they are deeper than 0.05 in f_{syn} in the previous stage, but we found that a significant number of them are deep because of the contamination. Among the 118 lines in MB99, for example, 53 and 25 were rejected in the cases of Arcturus and μ Leo, respectively, considering the depths in $f_{syn}^{\dagger} - f_{syn}$. Then, we rejected lines with $\beta_1 > 0.3$ or $\beta_2 > 1$; 8 and 21 lines were rejected in the cases of Arcturus and μ Leo, respectively, although those lines are strong enough. Figure 3 shows examples of Fe I lines with different β_1 and β_2 values. We note that the selection in this section was made on the basis of synthetic spectra, and not observed ones. Some Fe I lines look isolated enough in synthetic spectra but turn out to be severely blended with neighboring strong lines that are not reproduced in the synthetic spectra (see Section 5.1). All of the abovementioned rejections were made independently for each combination of the line list (VALD3 or MB99) and the object (Arcturus or μ Leo).

Tables 2 and 3 list the selected lines, and Table 4 lists the number of the lines, N_1, for each combination of line list and object. Some lines were selected only for one of the two objects owing to the large difference in metallicity. Among the 97 selected lines from VALD3 (Table 2), 24 lines are weak only in Arcturus, while there are no lines, as expected, which are weak in μ Leo but strong enough in Arcturus. In contrast, 6 lines were rejected due to the blending for μ Leo only, and no lines selected for μ Leo show strong blends in Arcturus. The situation is similar for the 75 selected lines from MB99. 18 lines were rejected for Arcturus because they are weak in
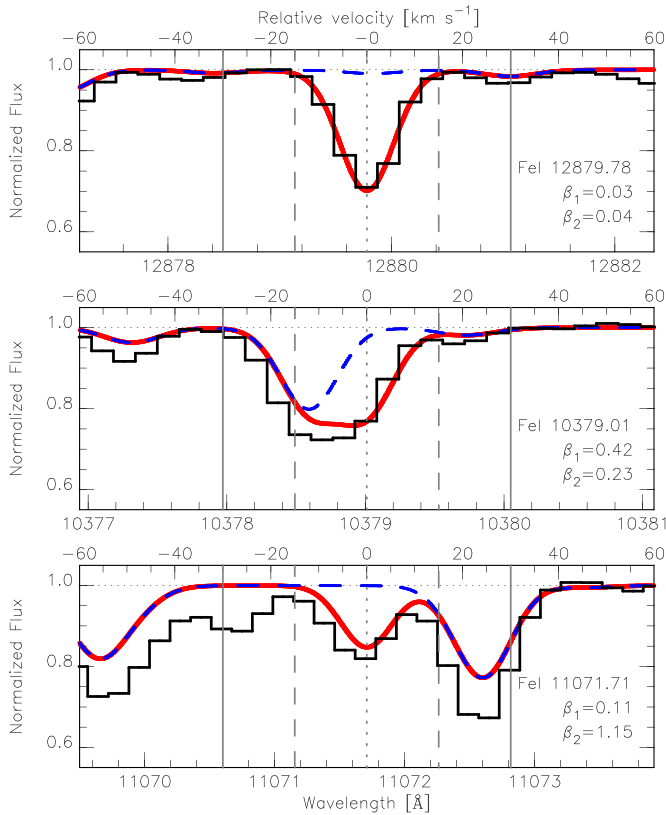
Figure 3. Comparisons between the observational spectrum (black) and the two synthetic spectra ($f_{\rm syn}$ by red solid curve and $f_{\rm syn}^{\dagger}$ by blue dashed curve; see the text for details) are illustrated for three Fe I lines seen in μ Leo as examples. The MB99 list was used for atomic lines in those synthetic spectra. The vertical lines indicate the central wavelength and the velocity ranges corresponding to the widths of $\Delta_1 = 30$ and $\Delta_2 = 60$ km s^{-1}. The three Fe I lines have different β_1 and β_2 values from each other, as labeled in the panels, and only the one in the top panel was selected for our abundance analysis according to the selection criteria of $\beta_1 < 0.3$ and $\beta_2 < 1$.

Table 2
List of Fe I Lines Selected from VALD3 and Abundances

Wavelength (Å)	EP (eV)	log gf (dex)	Arcturus (dex)	μ Leo (dex)
9117.1309	2.8581	−3.454	6.970	7.888
9118.8806	2.8316	−2.115	6.411	8.612
9146.1275	2.5881	−2.804	6.828	6.749
9210.0240	2.8450	−2.404	6.789	7.276
9602.1301	5.0117	−1.744	(w)	7.408
9653.1147	4.7331	−0.684	6.780	7.545
9657.2326	5.0856	−0.780	6.768	7.152
9738.5725	4.9913	+0.150	6.861	7.308
9753.0906	4.7955	−0.782	6.850	(*)
9791.6983	2.9904	−4.223	(w)	7.126
9800.3075	5.0856	−0.453	6.558	7.457
9811.5041	5.0117	−1.362	7.100	7.646
9820.2408	2.4242	−5.073	(w)	(*)
9861.7337	5.0638	−0.142	6.647	(b)
9868.1857	5.0856	−0.979	7.098	8.246
9889.0351	5.0331	−0.446	6.974	7.660
9937.0898	4.5931	−2.442	(w)	7.544
9944.2065	5.0117	−1.338	7.046	7.401
9980.4629	5.0331	−1.379	6.851	7.935
10041.472	5.0117	−1.772	(w)	7.958
10065.045	4.8349	−0.289	6.774	7.618
10081.393	2.4242	−4.537	6.995	7.602
10114.014	2.7586	−3.692	6.918	(b)
10145.561	4.7955	−0.177	6.947	(b)
10155.162	2.1759	−4.226	6.770	7.459

Note. These are the first 25 lines. Lines weaker than the limit 0.05 in depth in synthetic spectra, are flagged as (w), and lines that are blended too much are flagged as (b). The flag (*) indicates lines whose abundance could not be obtained or was rejected. See the details of the line selection in the text. The entire list is available as an ASCII file in the online journal.

(This table is available in its entirety in machine-readable form.)

$f_{\rm syn}^{\dagger} - f_{\rm syn}$, while no line selected for Arcturus is weak in μ Leo. Three lines were rejected because of blends in μ Leo, but no line selected for μ Leo was rejected owing to blends in Arcturus.

5. Measurement of Microturbulence and Metallicity

5.1. Bootstrap Method to Measure ξ and log $\epsilon_{\rm Fe}$

We determined the iron abundance (log $\epsilon_{\rm Fe}$) and the microturbulence (ξ) simultaneously for each combination of object (Arcturus or μ Leo) and line list (VALD3 or MB99) as follows. The basic assumption of the method is that the log $\epsilon_{\rm Fe}$ values should be independent of line strength, as is often assumed in the classical method of abundance analysis (see the Introduction).

We measured the log $\epsilon_{\rm Fe}$ of each Fe I line for 21 different ξ values from 0.5 to 2.5 km s^{-1} with a step of 0.1 km s^{-1}. For each combination of line and ξ, log $\epsilon_{\rm Fe}$ was estimated by a least-squares fit to a small part of the spectrum around the line using MPFIT (Takeda 1995), which is implemented in SPTOOL. Each MPFIT run was performed with a fixed ξ. We used a fitting window, $[\lambda_c - \Delta_2/2 : \lambda_c + \Delta_2/2]$, where λ_c is the central wavelength of each line and Δ_2 is the wavelength shift corresponding to a redshift of 60 km s^{-1}, as Equation (1). MPFIT searches for an optimized solution by treating the

following as free parameters: log $\epsilon_{\rm Fe}$, the width of Gaussian line broadening (including macroturbulence and instrumental broadening), and a small wavelength offset $\Delta\lambda$, which compensates for any remaining errors in the wavelength calibration and in the correction of the redshift of the target. We thus obtained log $\epsilon_{\rm Fe}$ values for the grid of 21 ξ values for individual Fe I lines. The number of lines measured for each combination of line list and object is given as N_2 in Table 4. Note that MPFIT failed to give a solution for a few lines for μ Leo, namely, Fe I 11026.78, 11053.52, and 11135.96 Å from both line lists, Fe I 9753.09, 9820.24, 13145.07, and 11119.80 Å from VALD3 only, and Fe I 11715.49, and 13291.78 Å from MB99 only. Visual inspection of its observed spectrum around these lines suggests that they are blended by one or two other strong lines. Such cases could have been rejected based on the β_1 and β_2 indices, but the blends around the above lines were not reproduced by the synthetic spectra (on the basis of MB99 and VALD3). Four and three of these lines were rejected for Arcturus when we used VALD3 and MB99, respectively, because they were predicted to be weak, but for the other lines we obtained log $\epsilon_{\rm Fe}$ of Arcturus. In Tables 2 and 3, we include these lines for which MPFIT failed, marked with an asterisk (*), because they may still be useful in some cases or once the line lists have been improved to reproduce the spectra including the neighboring lines. The Fe I line at 13291.78 Å in the MB99 list was selected

Table 3
List of Fe I Lines Selected from MB99 and Abundances

Wavelength (Å)	EP (eV)	log gf (dex)	Arcturus (dex)	μ Leo (dex)
10019.79	5.48	−1.44	(w)	7.582
10032.86	5.51	−1.36	(w)	7.522
10041.47	5.01	−1.84	(w)	7.982
10065.05	4.84	−0.57	7.144	7.825
10081.39	2.42	−4.53	6.963	7.459
10114.02	2.76	−3.76	7.010	(b)
10145.57	4.80	−0.41	7.335	8.342
10155.16	2.18	−4.36	6.901	7.438
10167.47	2.20	−4.26	7.071	7.757
10195.11	2.73	−3.63	6.915	7.800
10216.32	4.73	−0.29	7.262	8.006
10218.41	3.07	−2.93	7.092	8.038
10230.78	5.87	−0.70	(w)	7.774
10265.22	2.22	−4.67	6.962	7.416
10307.45	4.59	−2.45	(w)	7.524
10340.89	2.20	−3.65	7.092	7.508
10347.96	5.39	−0.82	6.970	8.024
10353.81	5.39	−1.09	(w)	7.707
10395.80	2.18	−3.42	6.749	7.353
10401.72	3.02	−4.36	(w)	7.583
10435.36	4.73	−2.11	(w)	7.852
10452.75	3.88	−2.30	6.781	7.713
10469.66	3.88	−1.37	6.984	7.908
10532.24	3.93	−1.76	7.151	7.733
10555.65	5.45	−1.39	(w)	7.565

Note. These are the first 25 lines. The entire list is available as an ASCII file in the online journal. The meanings of the flags, (w), (b), and (*), are the same as in Table 2.

(This table is available in its entirety in machine-readable form.)

Table 4
Microturbulence and Iron abundance

Line list	N_1	N_2	ξ (km s^{-1})	log $\epsilon_{\rm Fe}$ (dex)	r
			Arcturus		
VALD3	73	67	$1.22^{-0.12}_{+0.12}$	$6.81^{+0.06}_{-0.06}$	−0.946
MB99	57	53	$1.20^{-0.11}_{+0.11}$	$7.01^{+0.04}_{-0.04}$	−0.875
			μ Leo		
VALD3	91	79	$1.16^{-0.24}_{+0.23}$	$7.62^{+0.11}_{-0.10}$	−0.909
MB99	72	63	$1.54^{-0.17}_{+0.17}$	$7.73^{+0.06}_{-0.05}$	−0.828

for μ Leo; however, MPFIT gives completely wrong log $\epsilon_{\rm Fe}$ values, higher than 10 dex. We found that this line is severely blended in the observed spectrum of μ Leo, but it looks fairly isolated in the synthetic spectrum. This inconsistency probably causes the absurd log $\epsilon_{\rm Fe}$ values. We, therefore, reject the MPFIT measurements of this line but include the line in Table 3 marked with the asterisk (*). These rejected lines are not included in N_2 in Table 4. Additionally, the lines with $X > -6$ are not used when we estimate the final iron abundances (Section 5.2), and those lines are not included in N_2 in the table.

We then used a bootstrap method to obtain not only the best estimates of ξ and log $\epsilon_{\rm Fe}$ but also respective errors. We repeatedly extracted N_2 randomly selected lines among the N_2 lines with (ξ, log $\epsilon_{\rm Fe}$) available. Note that for each bootstrap
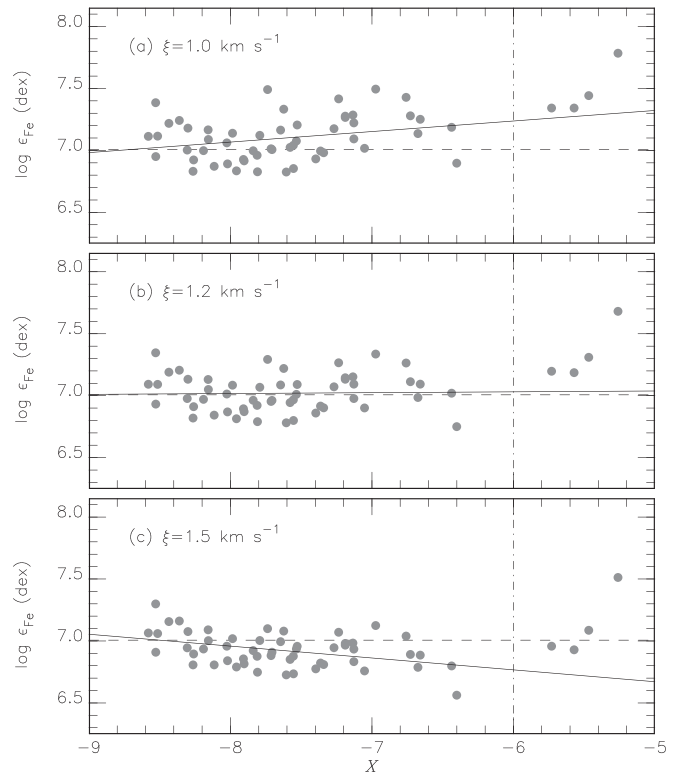

Figure 4. Dependency of log $\epsilon_{\rm Fe}$ on line strength indicated by X at different ξ values, (a) 1.0, (b) 1.2, and (c) 1.5 km s^{-1}. The solid line in each panel shows the linear fit to the (X, log $\epsilon_{\rm Fe}$) points at $X < -6$. This plot is for the combination of the MB99 line list and Arcturus. The Fe I lines with $X > -6$, indicated by the vertical line in each panel, were not used in the final (ξ, log $\epsilon_{\rm Fe}$) determination.

sample, each line may be selected more than once and some lines may be excluded.

For a given set of the (ξ, log $\epsilon_{\rm Fe}$) values for a bootstrap sample, we obtained the best estimates of ξ and log $\epsilon_{\rm Fe}$ as follows. First, we searched for ξ that leads to no trend of log $\epsilon_{\rm Fe}$ of individual lines against the line strength. We considered the X value introduced in Section 4 as a proxy of the line strength, and made a simple least-squares fit,

$$\log \epsilon_{\rm Fe} = aX + b, \qquad (4)$$

to calculate the trend, a, for each ξ of the grid. Figure 4 illustrates that lines with different strengths have different responses to ξ. Lines with large X values, but within the range of $X < -6$, tend to give smaller log $\epsilon_{\rm Fe}$ for larger ξ. This leads to a monotonic decrease in the slope a with increasing ξ. One can, thus, find a ξ that gives $a = 0$ by interpolating two neighboring ξ values where a turns from positive to negative. In Figure 4, a is almost zero at $\xi = 1.2$ km s^{-1} (panel b). The lines at $X > -6$ are biased toward higher log $\epsilon_{\rm Fe}$ values, and we will discuss their impact on the estimate of ξ and log $\epsilon_{\rm Fe}$ in Section 5.3. For the ξ obtained, we calculated log $\epsilon_{\rm Fe}$ for N_2 individual lines of the bootstrap sample by interpolating the grid points of (ξ, log $\epsilon_{\rm Fe}$) and took the average of the log $\epsilon_{\rm Fe}$ values. This gives the best estimate of (ξ, log $\epsilon_{\rm Fe}$) for the given bootstrap sample. We then took the median and also the 16th and 84th percentiles (as the $\pm 1\sigma$ range) in each of the histograms of ξ and log $\epsilon_{\rm Fe}$ values obtained after a large number of bootstrap samples. We repeated this procedure one
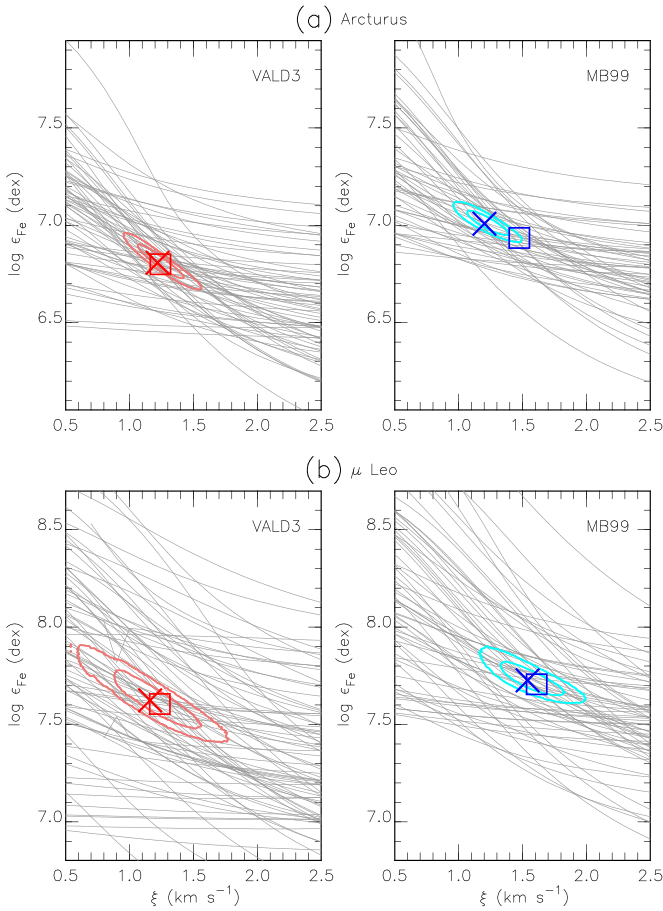
Figure 5. Contours for the density distribution of (ξ, $\log \epsilon_{Fe}$) obtained in the bootstrap simulation. The inner and outer contours show the ranges that include 68.26% (1σ) and 95.44% (2σ) of the 1,000,000 bootstrap samples. Four panels are given for the combinations of line lists (VALD3 and MB99) and targets (Arcturus and μ Leo). In each panel, gray curves indicate the dependency of $\log \epsilon_{Fe}$ for individual lines. The cross symbol indicates the best estimates that we obtained for each set (Table 4), and the open square indicates the estimates obtained with strong lines with $X > -6$ included (see Section 5.2).

million times ($N_b = 1,000,000$) in this study, and the best estimates of (ξ, $\log \epsilon_{Fe}$) are listed in Table 4 for each combination of the line list and object. We also calculated the correlation coefficient of the two parameters,

$$ r = \frac{\sum (\xi^i - \langle \xi \rangle)(\log \epsilon_{Fe}^i - \langle \log \epsilon_{Fe} \rangle)}{\sqrt{\sum (\xi^i - \langle \xi \rangle)^2} \sqrt{\sum (\log \epsilon_{Fe}^i - \langle \log \epsilon_{Fe} \rangle)^2}}, \quad (5) $$

where ξ^i and $\log \epsilon_{Fe}^i$ are the microturbulence and iron abundance obtained for each bootstrap sample, and $\langle \xi \rangle$ and $\langle \log \epsilon_{Fe} \rangle$ are their means (not medians). Each of the summations in Equation (5) takes the integer i for N_b lines, i.e., $1 \leqslant i \leqslant N_b$.

The contours in Figure 5 represent the distribution of (ξ, $\log \epsilon_{Fe}$) obtained in the bootstrap simulation. The large N_b was used mainly to obtain smooth contours in Figure 5, although we could obtain reasonably stable values including 1σ confidence intervals at around $N_b = 10,000$. There is a linear anticorrelation, as expected, between ξ and $\log \epsilon_{Fe}$, which shows that the errors in the two parameters are anticorrelated (see r in Table 4). We do not use r later in this paper, but it is a useful indicator of how much the measured $\log \epsilon_{Fe}$ depends on the ξ estimated. For example, r is expected to vary with the

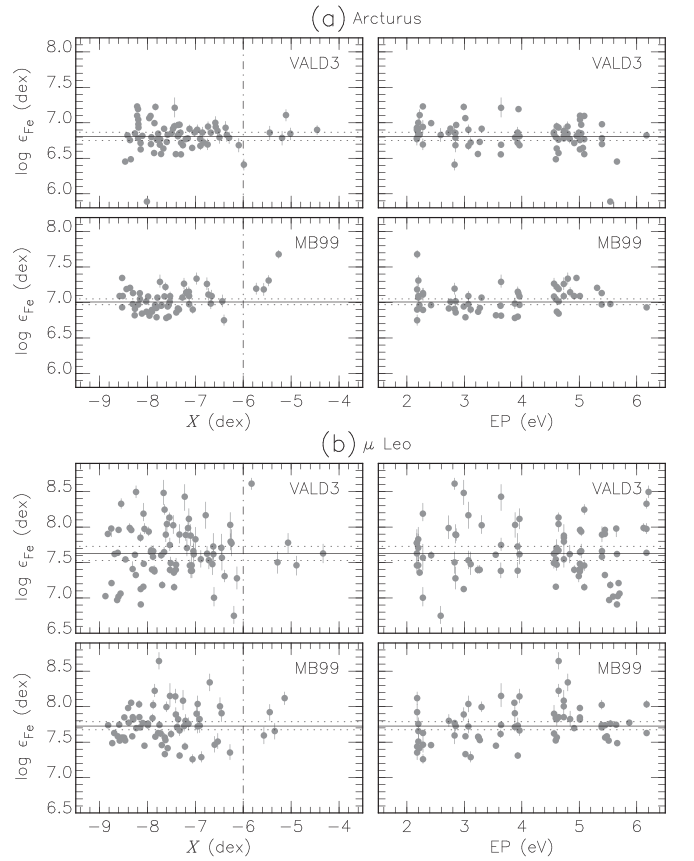**Figure 6.** $\log \epsilon_{Fe}$ values obtained for individual Fe I lines are plotted against the line strength indicator, X, on the left-hand side and against the excitation potential, EP, on the right-hand side. For each of the two targets (Arcturus in the upper panels and μ Leo in the lower panels), the results for the two line lists (VALD3 and MB99) are presented. The horizontal solid line and the dashed lines in each panel indicate the best estimate and 1σ confidence intervals for the combination of line list and target. The Fe I lines with $X > -6$, indicated by the vertical line in each panel, were not used in the final (ξ, $\log \epsilon_{Fe}$) determination.

proportion of strong lines. Using more weak lines would reduce the anticorrelation because the $\log \epsilon_{Fe}$ values of weak lines have a smaller dependency on ξ.

Now, we estimate $\log \epsilon_{Fe}$ values of individual lines with the best estimates of ξ that are given in Table 4. For each combination of object and line list, each Fe I line has 21 measurements of $\log \epsilon_{Fe}$ at different ξ values, and we interpolated $\log \epsilon_{Fe}$ values at the two grid points of ξ next to its best estimate. The $\log \epsilon_{Fe}$ values obtained for individual lines are listed in Table 2 for VALD3 and in Table 3 for MB99. In the two tables, lines weaker than the limit are flagged as (w), and lines that are blended too much are flagged as (b). Lines whose MPFIT measurements were unavailable or rejected were not used for the abundance analysis, but we include them in the tables with the (*) flag. Figure 6 plots the individual $\log \epsilon_{Fe}$ values against the X value and EP. For both objects, the X values of the measured lines are spread over a wide range, approximately between -9 and -5 dex. Such a wide range among the lines in the z', Y, and J bands is advantageous, for example, compared with a narrow range, -8.3 to -7.3 dex, covered by the H-band lines used by Smith et al. (2013). The $\log \epsilon_{Fe}$ shows little dependency on X as demanded in the analysis and also have no clear dependency on EP, indicating that the adopted T_{eff} are reasonable. The scatters of $\log \epsilon_{Fe}$ from individual lines are larger for μ Leo than for Arcturus. This is
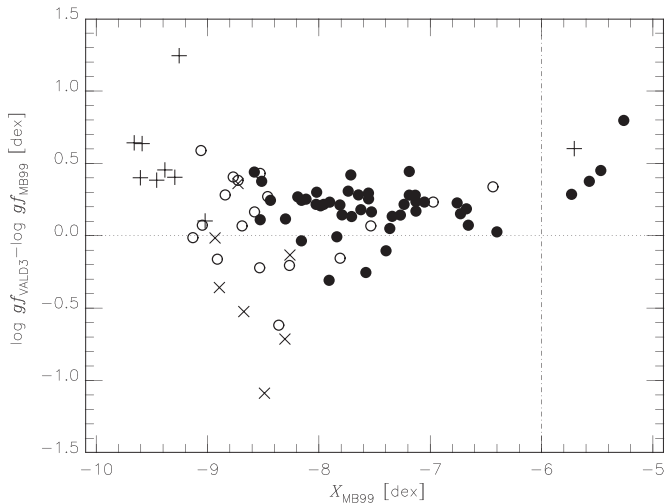
Figure 7. Comparison of the $\log gf$ values for the two line lists VALD3 and MB99. The filled circles indicate the lines used for all combinations of line list and target, and the open circles indicate those used for both line lists but for only one of the two targets, Arcturus or μ Leo. The $+$ and $\times$ symbols indicate the lines used in only one of the line lists ($+$ for VALD3 and $\times$ for MB99) for both targets. The temperature of Arcturus, $T_{\rm eff} = 4286$ K, and the $\log gf$ values for MB99 are used for calculating the X values (abscissa).

probably because the spectrum of μ Leo has stronger contaminating lines, especially CN lines, than Arcturus (McWilliam & Rich 1994; Smith et al. 2013), which makes it harder to trace the continuum.

5.2. Comparison between the Two Line Lists

There are a few differences between the estimates of $(\xi, \log \epsilon_{\rm Fe})$ obtained with the two line lists.

First, in Table 4, the standard errors for $\log \epsilon_{\rm Fe}$ from the two lists are similar to each other for Arcturus. The number of Fe I lines is larger for VALD3, but the measured $\log \epsilon_{\rm Fe}$ has a slightly larger scatter than for MB99, which is compensated by the larger N_2. For μ Leo, the scatter of $\log \epsilon_{\rm Fe}$ is rather large with VALD3 (Figure 6), and this leads to a larger standard error even with a larger number of Fe I lines.

Second, the resultant $\log \epsilon_{\rm Fe}$ values for MB99 are slightly higher than those obtained for VALD3. In fact, there is a systematic offset in the $\log gf$ values between the two line lists (Figure 7). The systematic offset, ~ 0.2 dex, approximately corresponds to the difference in $\log \epsilon_{\rm Fe}$ for Arcturus obtained with VALD3 and MB99. In contrast, the corresponding difference in the case of μ Leo is smaller. Although the offsets in the $\log gf$ have a direct impact on the $\log \epsilon_{\rm Fe}$ estimation, the different ξ values obtained for μ Leo with the two lists (larger ξ with MB99 than VALD3) partly compensate for this systematic offset.

Finally, the final estimates depend slightly on whether very strong lines with $X > -6$ are used or not. In Figure 7, very strong lines clearly show a systematic tilt. These strong lines have an impact on the slopes, e.g., seen in Figure 4. The lower $\log gf$ values of the stronger lines in MB99 would give higher $\log \epsilon_{\rm Fe}$ values with a fixed ξ, but this would also cause a tilt in Figure 4. A larger ξ is therefore required so that $\log \epsilon_{\rm Fe}$ values of strong and weak lines get balanced. While this is an important difference between the two line lists, generally speaking, it is suggested that using very strong lines often introduces complications such as non-LTE effects

into a chemical abundance analysis (e.g., Kovtyukh & Andrievsky 1999; Gratton et al. 2006; Takeda et al. 2013). Based on synthetic spectra, we found that, in the case of lines with $X \gtrsim -6$, the line core does not grow any more with increasing metallicity and the damping wing starts to contribute to the EW at around the solar metallicity. If we run the bootstrap method with the same lines but including those with $X > -6$, we obtain moderately different results for the MB99 list, as illustrated in Figure 5. Four lines from MB99 have $X > -6$, and including them leads to higher ξ and lower $\log \epsilon_{\rm Fe}$ values: $(\xi, \log \epsilon_{\rm Fe}) = (1.47 \pm 0.18, 6.94 \mp 0.05)$ for Arcturus and $(1.61 \pm 0.16, 7.71 \mp 0.06)$ for μ Leo. The changes caused by including the strongest lines are marginally significant, $1-2\sigma$, for the former but are negligible for the latter. Figure 6 shows that one line, Fe I λ 11973.04, with the largest $(X, \log \epsilon_{\rm Fe})$ has a particularly strong impact on the slope in the X versus $\log \epsilon_{\rm Fe}$ diagram for Arcturus with MB99. The same line gives $\log \epsilon_{\rm Fe} \sim 8.10$ dex, which is also higher than the average, for μ Leo. However, the scatter of $\log \epsilon_{\rm Fe}$ from lines within the low-X range is large, which explains the relatively small effect of including the high-X lines for μ Leo. In contrast, six VALD3 lines that we selected have $X > -6$, but including them has a negligible impact on the $(\xi, \log \epsilon_{\rm Fe})$ measurements. For VALD3, the Fe I λ 11973.046 line leads to $\log \epsilon_{\rm Fe}$ values that are very close to the average abundances from other lines for both Arcturus and μ Leo. This line corresponds to the rightmost point in Figure 7 and has a very large difference, 0.8 dex, between the $\log gf$ values in the two line lists. Considering these complications, we decided to adopt the $(\xi, \log \epsilon_{\rm Fe})$ values obtained without the lines at $X > -6$ as our best estimates. Although the $\log \epsilon_{\rm Fe}$ from individual lines depend on ξ as described above, we found that the [Fe/H] obtained in different works are not correlated with ξ (Figure 8). This is probably because systematic differences in previous works, such as differences in line lists and atmosphere models, introduced a scatter larger than the expected correlation between the two parameters.

5.3. Effects of Stellar Parameters on Metallicity

Here, we estimate how much the uncertainties in the stellar parameters, $T_{\rm eff}$, $\log g$, and [M/H], affect the estimates of $\log \epsilon_{\rm Fe}$. We adopt the errors in these parameters from Heiter et al. (2015), as given in Table 1. To evaluate the effect of changing the three parameters, we added positive and negative offsets to each parameter in the atmosphere models one by one. For each offset, we ran MPFIT and obtained $\log \epsilon_{\rm Fe}$ for the N_2 lines and calculated their means. We did not use the bootstrap method described in Section 5.1 for this step because we need to estimate the effect of a parameter at a fixed ξ. Then, we compared the above means with the counterparts of the mean $\log \epsilon_{\rm Fe}$ with the stellar parameters in Table 1. This gives the offsets in $\log \epsilon_{\rm Fe}$, $\Delta(T_{\rm eff})$, $\Delta(\log g)$, and $\Delta([M/H])$, as a result of changing the stellar parameters (Table 5).

For both objects and for both line lists, we found that varying the temperature or the gravity gives rather tiny changes in $\log \epsilon_{\rm Fe}$. Synthetic spectra with the same parameters but an offset of 50 K in $T_{\rm eff}$ or an offset of ± 0.1 dex in $\log g$ do not actually show any noticeable changes in the Fe I lines. The $\Delta([M/H])$ is larger compared with these two. The $\Delta([M/H])$ of Arcturus is smaller than that of μ Leo. We believe that this is simply because the $\sigma[M/H]$ of Arcturus is smaller than that of

Table 5
Effects of Stellar Parameters on Iron Abundance

Line list	$\sigma T_{\rm eff}$ (K)	$\Delta(T_{\rm eff})$ (dex)	$\sigma \log g$ (dex)	$\Delta(\log g)$ (dex)	σ [M/H] (dex)	$\Delta([{\rm M/H}])$ (dex)	σ_ξ (km s^{-1})	$\Delta_{\rm b}^+$ (dex)	$\Delta_{\rm b}^-$ (dex)	$\Delta_{\rm total}$ (dex)
					Arcturus					
VALD3	±35	±0.006	±0.06	±0.008	±0.08	±0.025	±0.12	-0.058	$+0.059$	0.064
MB99	±35	±0.007	±0.06	±0.009	±0.08	±0.021	±0.11	-0.040	$+0.043$	0.048
					μ Leo					
VALD3	±60	∓0.003	±0.09	±0.008	±0.15	±0.052	$^{+0.24}_{-0.23}$	-0.095	$+0.106$	0.114
MB99	±60	∓0.004	±0.09	±0.017	±0.15	±0.040	±0.17	-0.052	$+0.061$	0.071

Note. The σ_p and the $\Delta(p)$ indicate the error of stellar parameter p and its effect on $\log \epsilon_{\rm Fe}$, where p takes $T_{\rm eff}$, $\log g$, or [M/H]. The $\Delta_{\rm b}^\pm$ indicate the error of $\log \epsilon_{\rm Fe}$ from the bootstrap method. In the last column, the $\Delta_{\rm total}$ is the total uncertainty (see details in the text).
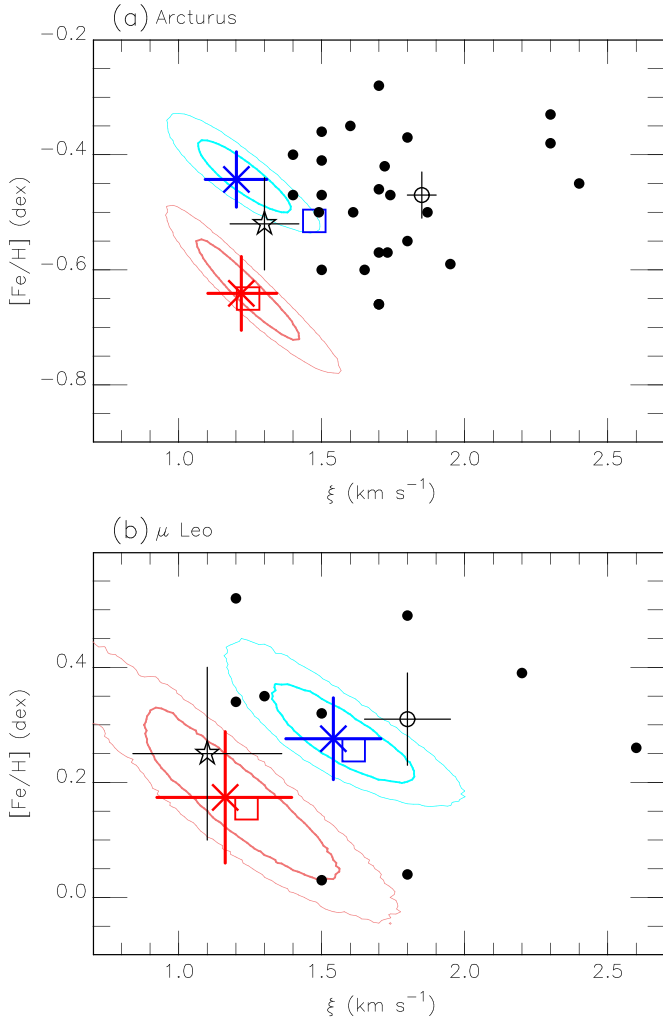

Figure 8. Comparison of our estimates of ξ and [Fe/H] with previous estimates. The contours, cross symbols, and open squares are the same as in Figure 5. The results for VALD3 and MB99 are illustrated in red and blue, respectively. The total errors in Table 5 are added to the crosses. Two recent results in the literature are shown with error bars: Smith et al. (2013) and Jofré et al. (2014) indicated by an open circle and a star symbol, respectively. The filled circles indicate the other previous estimates that we compiled in Figure 2 except those without the microturbulence explicitly given.

μ Leo. We combine the Δ values with the confidence intervals of $\log \epsilon_{\rm Fe}$ estimated by the bootstrap method, the $\Delta_{\rm b}$, in Table 5. Note that the $\Delta_{\rm b}$ correlated with ξ include other errors,

e.g., observational errors in the spectra and errors in $\log gf$. Combining the above errors, we can estimate the total error as

$$\Delta_{\rm total} = \sqrt{\Delta_{\rm b}^2 + \Delta(T_{\rm eff})^2 + \Delta(\log g)^2 + \Delta([{\rm M/H}])^2}, \quad (6)$$

which is given in Table 5. Here, we ignored the covariant terms. The previous estimates that we compiled in Figure 2 show no clear correlation between any two of the four parameters, $T_{\rm eff}$, $\log g$, [Fe/H], or ξ.

5.4. Comparison with Previous Results

Figure 8 plots the scaled metallicity [Fe/H], where the solar $\log \epsilon_{\rm Fe}$ is assumed to be 7.45 dex, against ξ. We compared our iron abundances with those in previous papers (an open circle: Smith et al. 2013, a star: Jofré et al. 2014, filled circles: the others) that we compiled in Figure 2 except those without the microturbulence explicitly given. Our total errors are comparable with the errors estimated by Smith et al. (2013) and Jofré et al. (2014). Within the errors and scatters of [Fe/H] in the literature, our metallicities based on the z', Y, and J bands spectra agree very well with previous estimates. The metallicities estimated with MB99 show better agreement with previous estimates than those with VALD3. Considering also that the scatters in Figure 6 are smaller with MB99, we believe that the $\log gf$ values of MB99 are better than those of VALD3 for chemical abundance analyses.

6. Concluding Remarks

We used the $z'YJ$ band high-resolution spectra of Arcturus and μ Leo, obtained with WINERED, to estimate the microturbulence and iron abundance with a precision similar to that of previous results from spectra at different wavelengths. Our lists of Fe I lines in the 0.91–1.33 μm range will be useful for obtaining the precise metallicities of stars obscured by severe interstellar extinction compared with the optical regime, for which the extinction is stronger. For many objects in the Galactic disk found in recent infrared surveys, this new wavelength window may be ideal for detailed abundance analyses. One of the major error sources is the uncertainty in ξ in various studies, including ours, based on spectra at different wavelengths from the optical (e.g., Table 3 of Jofré et al. 2014) to the H band (e.g., Table 7 of Smith et al. 2013). Furthermore, how to determine the microturbulence and its error is not established or straightforward. The bootstrap method that we demonstrated in this paper can give quantitative estimates of the microturbulence and its error. The error in microturbulence is 0.11–0.24 km s^{-1} for each combination of target and line list.

The obtained microturbulences are consistent with those that were estimated or assumed in previous studies on the same targets. Note, however, that using different line lists (or different sets of lines) can result in slightly different microturbulences depending especially on the $\log gf$ values of strong lines used in the analysis. The very strong lines ($X > -6$) were rejected because these lines are likely to introduce problems into a chemical abundance analysis due to severe saturation, non-LTE effects, contribution of EW from the damping wing, and so on. Considering the comparison of our estimates with previous ones in addition to the scatters of $\log \epsilon_{\mathrm{Fe}}$, we adopt the measurements with the Fe I lines selected from MB99 as our best estimates: (ξ, $\log \epsilon_{\mathrm{Fe}}$) = (1.20 ± 0.11 km s^{-1}, 7.01 ± 0.05 dex) and (1.54 ± 0.17 km s^{-1}, 7.73 ± 0.07 dex) for Arcturus and μ Leo, respectively.

ORCID iDs

Yuji Ikeda ⬤ https://orcid.org/0000-0003-2380-8582
Hiroaki Sameshima ⬤ https://orcid.org/0000-0001-6401-723X
Natsuko Izumi ⬤ https://orcid.org/0000-0003-1604-9127
Misaki Mizumoto ⬤ https://orcid.org/0000-0003-2161-0361
Takuji Tsujimoto ⬤ https://orcid.org/0000-0002-9397-3658

References

Anders, E., & Grevesse, N. 1989, GeCoA, 53, 197
Bell, R. A., Edvardsson, B., & Gustafsson, B. 1985, MNRAS, 212, 497
Boeche, C., & Grebel, E. K. 2016, A&A, 587, A2
Britavskiy, N. E., Andrievsky, S. M., Tsymbal, V. V., et al. 2012, A&A, 542, A104
Brown, J. A., & Wallerstein, G. 1992, AJ, 104, 1818
Bruntt, H., Frandsen, S., & Thygesen, A. O. 2011, A&A, 528, A121
Carr, J. S., Sellgren, K., & Balachandran, S. C. 2000, ApJ, 530, 307
Castro, S., Rich, R. M., McWilliam, A., et al. 1996, AJ, 111, 2439
Cunha, K., & Smith, V. V. 2006, ApJ, 651, 491
Davies, B., Origlia, L., Kudritzki, R.-P., et al. 2009a, ApJ, 694, 46
Davies, B., Origlia, L., Kudritzki, R.-P., et al. 2009b, ApJ, 696, 2014
Edvardsson, B. 1988, A&A, 190, 148
Fukue, K., Matsunaga, N., Yamamoto, R., et al. 2015, ApJ, 812, 64
Fulbright, J. P., McWilliam, A., & Rich, R. M. 2006, ApJ, 636, 821
García Pérez, A. E., Allende Prieto, C., Holtzman, J. A., et al. 2016, AJ, 151, 144
Gonzalez, G., & Wallerstein, G. 1998, AJ, 116, 765
Gratton, L., Gaudenzi, S., Rossi, C., & Gratton, R. G. 1982, MNRAS, 201, 807
Gratton, R., Bragaglia, A., Carretta, E., & Tosi, M. 2006, ApJ, 642, 462
Gratton, R. G., & Sneden, C. 1990, A&A, 234, 366
Grevesse, N., Asplund, M., & Sauval, A. J. 2007, SSRv, 130, 105
Heiter, U., Jofré, P., Gustafsson, B., et al. 2015, A&A, 582, A49
Hekker, S., & Meléndez, J. 2007, A&A, 475, 1003
Hill, V. 1997, A&A, 324, 435
Holtzman, J. A., Hasselquist, S., Shetrone, M., et al. 2018, AJ, 156, 125
Ikeda, Y., Kobayashi, N., Kondo, S., et al. 2016, Proc. SPIE, 9908, 99085Z
Jofré, P., Heiter, U., Soubiran, C., et al. 2014, A&A, 564, A133
Kovtyukh, V. V., & Andrievsky, S. M. 1999, A&A, 351, 597
Kurucz, R. L. 1993, Kurucz CD-ROM (Cambridge, MA: Smithsonian Astrophysical Observatory)
Kurucz, R. L., & Bell, B. 1995, Kurucz CD-ROM (Cambridge, MA: Smithsonian Astrophysical Observatory)
Kyrolainen, J., Tuominen, I., Vilhu, O., & Virtanen, H. 1986, A&AS, 65, 11
Lecureur, A., Hill, V., Zoccali, M., et al. 2007, A&A, 465, 799
Leep, E. M., Wallerstein, G., & Oke, J. B. 1987, AJ, 93, 338
Luck, R. E., & Challener, S. L. 1995, AJ, 110, 2968
Luck, R. E., & Heiter, U. 2005, AJ, 129, 1063
Maeckle, R., Holweger, H., Griffin, R., & Griffin, R. 1975, A&A, 38, 239
Magain, P. 1984, A&A, 134, 189
Majewski, S. R., et al. 2017, AJ, 154, 94
McWilliam, A. 1990, ApJS, 74, 1075
McWilliam, A., & Rich, R. M. 1994, ApJS, 91, 749
Meléndez, J., Asplund, M., Alves-Brito, A., et al. 2008, A&A, 484, L21
Meléndez, J., & Barbuy, B. 1999, ApJS, 124, 527
Mészáros, S., Allende Prieto, C., Edvardsson, B., et al. 2012, AJ, 144, 120
Ness, M., Hogg, D. W., Rix, H.-W., Ho, A. Y. Q., & Zasowski, G. 2015, ApJ, 808, 16
Oinas, V. 1974, ApJS, 27, 405
Origlia, L., Oliva, E., Maiolino, R., et al. 2013, A&A, 560, A46
Origlia, L., Oliva, E., Sanna, N., et al. 2016, A&A, 585, A14
Peterson, R. 1976, ApJS, 30, 61
Peterson, R. C., Dalle Ore, C. M., & Kurucz, R. L. 1993, ApJ, 404, 333
Ramírez, I., & Allende Prieto, C. 2011, ApJ, 743, 135
Ramírez, I., Allende Prieto, C., & Lambert, D. L. 2007, A&A, 465, 271
Ramírez, I., Allende Prieto, C., & Lambert, D. L. 2013, ApJ, 764, 78
Ryabchikova, T., et al. 2015, PhyS, 90, 054005
Ryde, N., Edvardsson, B., Gustafsson, B., et al. 2009, A&A, 496, 701
Ryde, N., Gustafsson, B., Edvardsson, B., et al. 2010, A&A, 509, A20
Ryde, N., Schultheis, M., Grieco, V., et al. 2016, AJ, 151, 1
Sameshima, H., Matsunaga, N., Kobayashi, N., et al. 2018, PASP, 130, 074502
Sheffield, A. A., Majewski, S. R., Johnston, K. V., et al. 2012, ApJ, 761, 161
Shetrone, M., Bizyaev, D., Lawler, J. E., et al. 2015, ApJS, 221, 24
Smith, G., & Ruck, M. J. 2000, A&A, 356, 570
Smith, V. V., Cunha, K., Shetrone, M. D., et al. 2013, ApJ, 765, 16
Sneden, C., Kraft, R. P., Langer, G. E., Prosser, C. F., & Shetrone, M. D. 1994, AJ, 107, 1773
Takeda, Y. 1995, PASJ, 47, 287
Takeda, Y., Kaneko, H., Matsumoto, N., et al. 2009, PASJ, 61, 563
Takeda, Y., Kang, D.-I., Han, I., Lee, B.-C., & Kim, K.-M. 2013, MNRAS, 432, 769
Taniguchi, D., et al. 2018, MNRAS, 473, 4993
Thévenin, F., & Idiart, T. P. 1999, ApJ, 521, 753
Thygesen, A. O., Frandsen, S., Bruntt, H., et al. 2012, A&A, 543, A160
Tomkin, J., & Lambert, D. L. 1999, ApJ, 523, 234
Worley, C. C., Cottrell, P. L., Freeman, K. C., & Wylie-de Boer, E. C. 2009, MNRAS, 400, 1039